CHAPTER 4

RESULTS AND DISCUSSION (PART I):

PREPARATION AND CHARACTERIZATION OF (1-*x*)PZT–*x*BDT SYSTEM

In this chapter, the results of (1-*x*)$Pb(Zr_{0.52}Ti_{0.48})O_3$–*x*$Bi_{3.25}Dy_{0.75}Ti_3O_{12}$ (when *x* = 0, 0.1, 0.3, 0.5, 0.7, 0.9 and 1.0) system were analyzed and discussed in both powder and ceramic forms. Phase formation, structure, processing relationships are brought out and discussed. As the first stage, it is focused initially on the preparation of $Pb(Zr_{0.52}Ti_{0.48})O_3$ (PZT) and $Bi_{3.25}Dy_{0.75}Ti_3O_{12}$ (BDT) powders. Then, these powders were used as the starting materials for fabricating the ceramics in the (1-*x*)PZT–*x*BDT system. Finally, phase formation, densification, microstructures, dielectric properties, ferroelectric properties and fatigue behaviors of the ceramics PZT–BDT system were investigated.

4.1 PZT, BDT and PZT–BDT powders

4.1.1 Phase analysis of PZT powders

The PZT powder was calcined for 2 h with a heating/cooling rate 5°C/min in air at various calcination temperatures between 700-900°C. All calcined powders were characterized by X-ray diffraction patterns (XRD). The XRD patterns of the calcined powders are shown in Figure 4.1, with the corresponding ICSD patterns also shown.

At the calcination temperature of 700°C, the starting chemicals (PbO, ZrO_2 and TiO_2) did not completely react to form single-phase powder. Upon calcination at 750-900°C, the XRD patterns indicate the formation of $Pb(Zr_{0.52}Ti_{0.48})O_3$ (PZT). They indicated the formation of two phases of tetragonal and rhombohedral phases. These can be matched with ICSD file numbers 92059 [102] and 97060 [103] of $Pb(Zr_{0.52}Ti_{0.48})O_3$ for the tetragonal and rhombohedral phases, respectively. It is well known that the variation in composition may lead to a diffuse morphotropic phase boundary (MPB) between the tetragonal and rhombohedral phases which could explain enhanced properties [104, 105]. The most obvious different between the patterns for tetragonal and rhombohedral PZT phases concerns the presence of a splitting of (002)/(200) peak at 2θ about 43-45° for the tetragonal phase. The experimental work carried out here suggested that the optimal calcination condition for the single-phase PZT was 800°C for 2 h with a heating/cooling rate of 5°C/min.

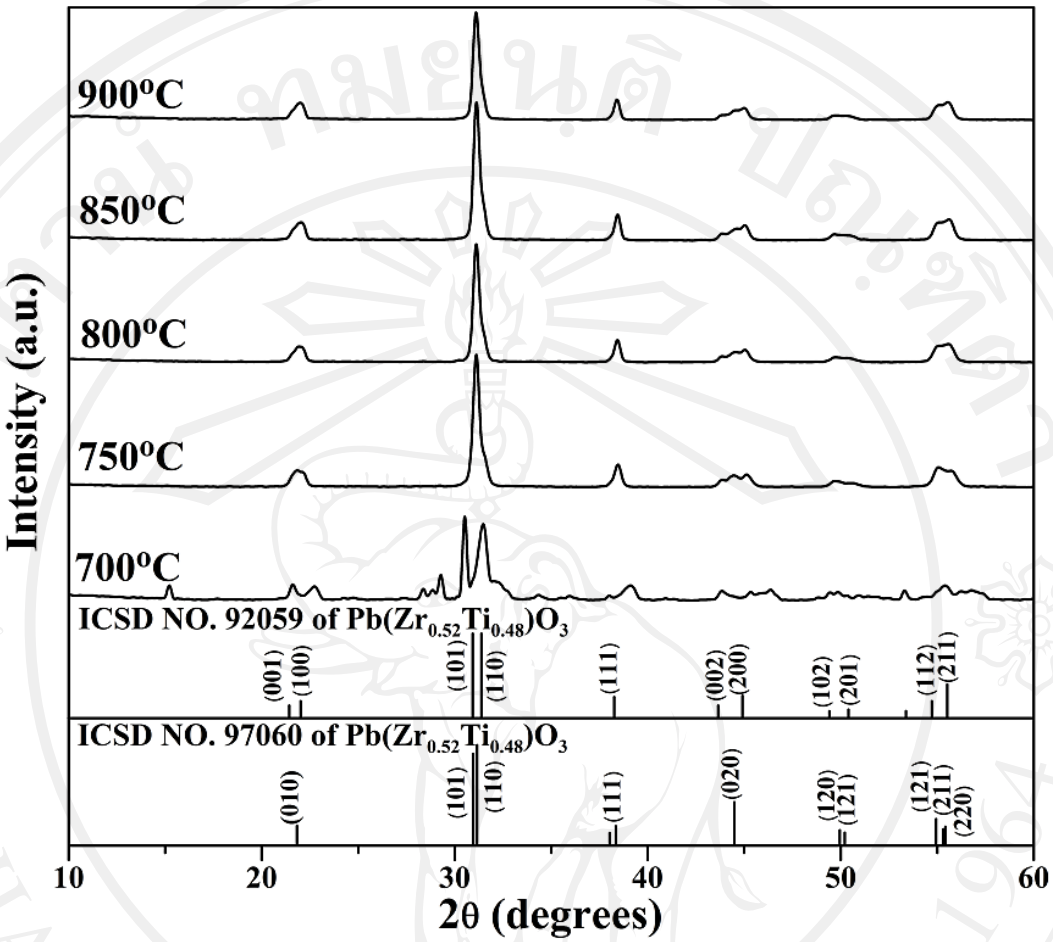

Figure 4.1 X-ray diffraction patterns of $Pb(Zr_{0.52}Ti_{0.48})O_3$ (PZT) powder calcined at 700-900°C.

4.1.2 Phase analysis of BDT powders

The BDT powder was calcined for 4 h with a heating/cooling rate 5°C/min at various temperatures (500-900°C). Figure 4.2 shows the XRD patterns of the calcined powder. The results revealed that at calcination temperature 500°C, the starting chemicals did not completely react to form single-phase powder. As the calcination temperature increased to 600-850°C, the BDT phase was already formed, however, the pattern of incompletely reacted Dy_2O_3 phase was still obtained. Upon the

calcination temperature at 900°C, the patterns of single-phase BDT were obtained. The BDT phase was indexable according to an orthorhombic phase which could be matched with ICSD file number 87810 of $Bi_4Ti_3O_{12}$ [106]. From the results, it can be seen that the single phase of BDT powder was also successfully obtained at a calcination temperature 900°C for 4 h with a heating/cooling rate 5°C/min.

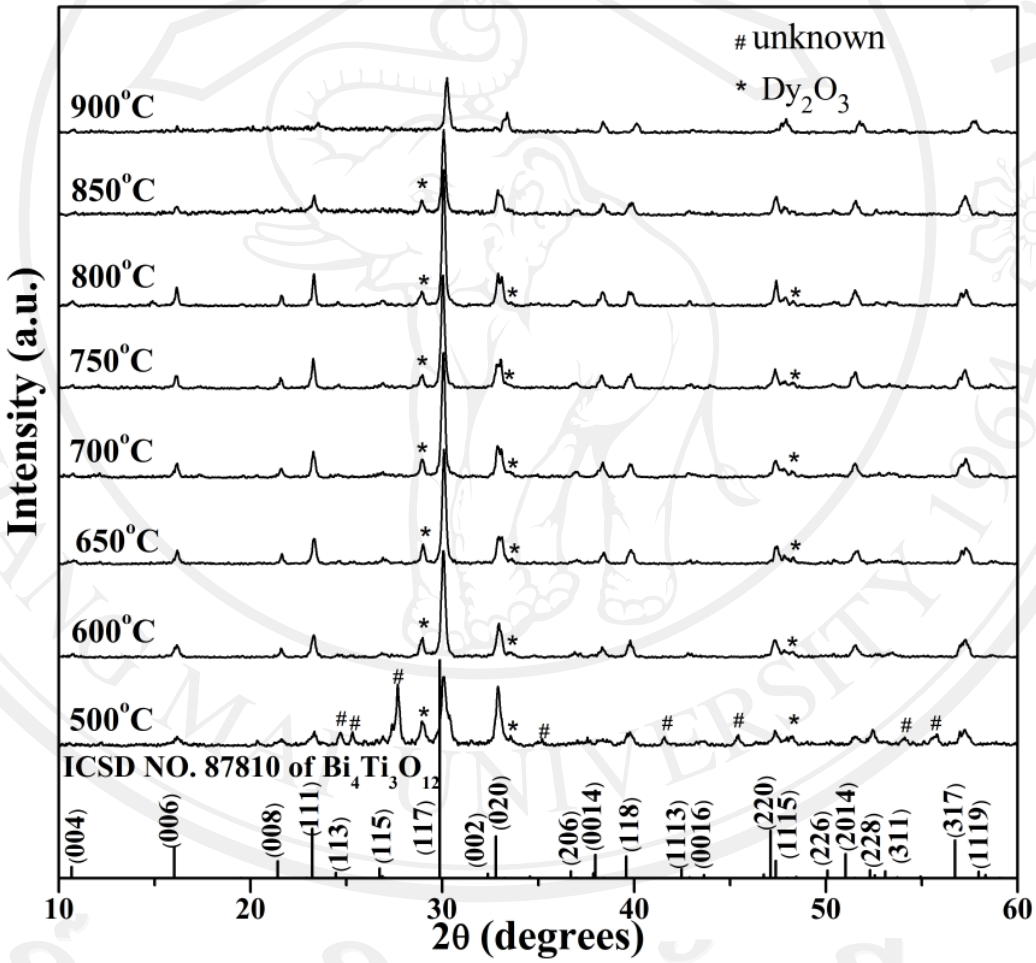

Figure 4.2 X-ray diffraction patterns of $Bi_{3.25}Dy_{0.75}Ti_3O_{12}$ (BDT) powder calcined at 500-900°C.

4.1.3 Phase analysis of (1-*x*)PZT–*x*BDT powders

From the results, the mixed powders of PZT and BDT were calcined at 800°C for 2 h and 900°C for 4 h with a heating cooling rate 5°C/min, respectively. The calcined powders of PZT and BDT were mixed to produce the powder mixture of (1-*x*)PZT–*x*BDT (*x* = 0, 0.1, 0.3, 0.5, 0.7, 0.9 and 1.0). The mixtures were characterized by XRD analysis, as shown in Figure 4.3. The patterns shows that the PZT powder was near morphotropic phase boundary (MPB) consisted of tetragonal phase (matched with ICSD file number 92059 of $Pb(Zr_{0.52}Ti_{0.48})O_3$ [102]) and rhombohedral phase (matched with ICSD file number 97060 of $Pb(Zr_{0.52}Ti_{0.48})O_3$ [103]). The BDT powder was identified as a single-phase material having an orthorhombic structure could be matched with ICSD file number 87810 of $Bi_4Ti_3O_{12}$ [106]. For the other compositions, all X-ray patterns show peaks of two-phase mixture corresponding to relative amount of each phase.

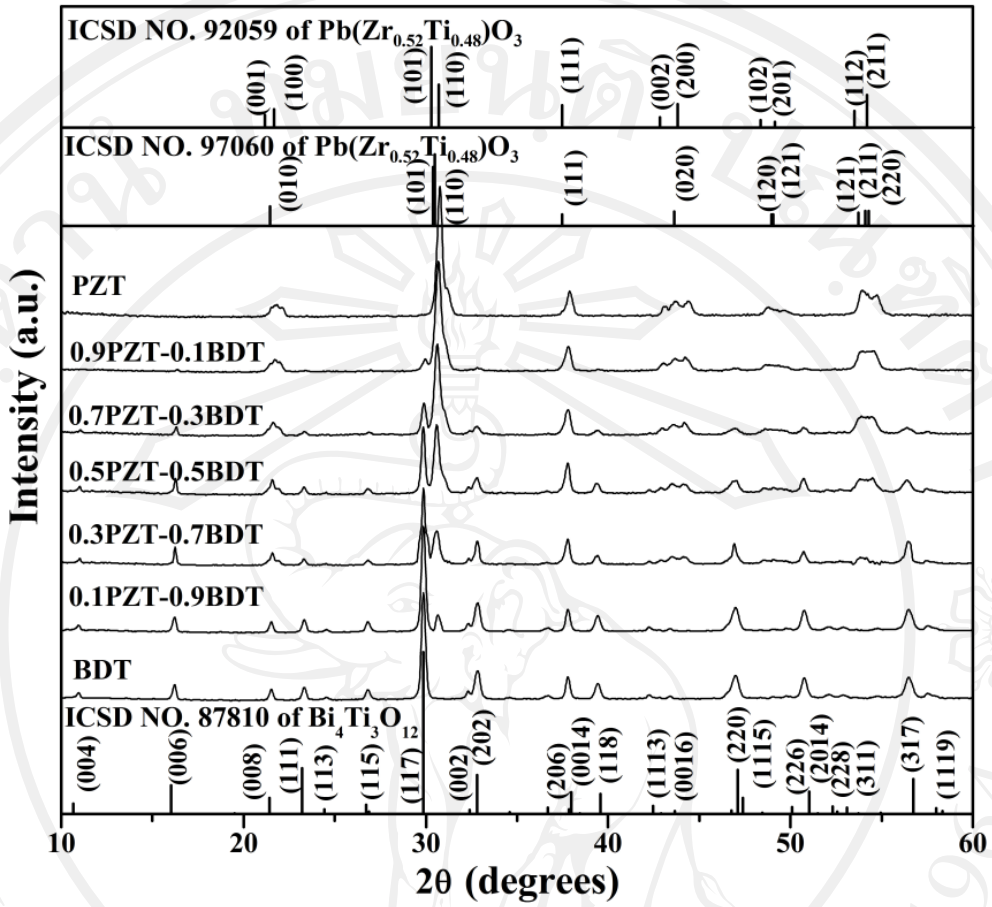

Figure 4.3 X-ray diffraction patterns of (1-*x*)PZT–*x*BDT powders.

4.2 PZT–BDT ceramics

After preparation of (1-*x*)PZT–*x*BDT powders, attempts to fabricate of high quality ceramics were carried out. Each mixture was pressed into pellet with an addition of 3 wt% polyvinyl alcohol (PVA) as a binder. These pellets were covered with their own powders and sintered at various sintering temperature between 950-1100°C for 4 h in air with a heating/cooling rate 5°C/min. The (1-*x*)PZT–*x*BDT ceramics were fabricated and fully characterized which were focused on phase formation, microstructure, dielectric properties, ferroelectric properties and fatigue behavior.

4.2.1 Densification of PZT–BDT ceramics

In this section, densification of the (1-*x*)PZT–*x*BDT ceramics sintered at various sintering temperaturesis investigated using Archimedes' method. Densification behavior of (1-*x*)PZT–*x*BDT ceramics sintered at temperature ranging from 950-1100°C are shown in Figure 4.4. Variation density with different sintering temperatures of all samples showed similar tendencies. The bulk density increased with an increase in temperature from 950°C and reached a maximum value at 1000°C for all compositions. At sintering temperature higher than 1000°C, the density was found to decrease. Moreover, the samples started to melt and caused the pellets to agglomerate with covered powder into hard irregular shaped solids. The reason for this result can be explained that probably some compounds (i.e., PbO and Bi_2O_3) melted and volatilized during the sintering process due to their lower melting points PbO~ 888°C [107] and Bi_2O_3 ~ 825°C [108] compared to the sintering temperatures employed in this study.

In this study, therefore, the optimum sintering temperature of (1-*x*)PZT–*x*BDT ceramic was found to be 1000°C for 4 h with a heating/cooling rate 5°C/min whose density values are also shown in Table 4.1. The highest density was achieved at 0.9PZT–0.1BDT ceramic (7.72 g/cm^3). Further increase the content of BDT gradually decreased densities of the ceramics.

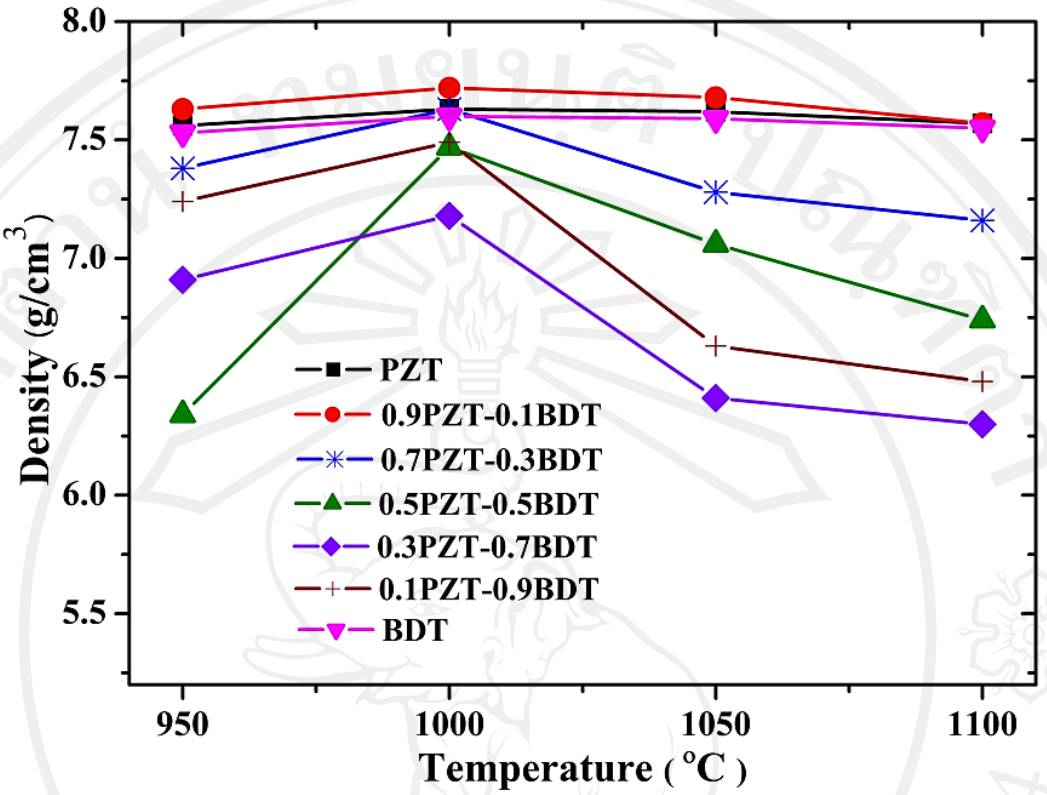

Figure 4.4 Density of (1-*x*)PZT–*x*BDT ceramics sintered at various temperatures.

Table 4.1 Densities of (1-*x*)PZT–*x*BDT ceramics sintered at 1000°C.

(1-*x*)PZT–*x*BDT	Density (g/cm^3)
PZT	7.63 ± 0.03
0.9PZT–0.1BDT	7.72 ± 0.02
0.7PZT–0.3BDT	7.62 ± 0.03
0.5PZT–0.5BDT	7.47 ± 0.03
0.3PZT–0.7BDT	7.18 ± 0.01
0.1PZT–0.9BDT	7.49 ± 0.01
BDT	7.60 ± 0.05

4.2.2 Phase analysis of PZT–BDT ceramics

X-ray diffraction patterns of (1-*x*)PZT–*x*BDT ceramics sintered at 1000°C for 4 h with a heating/cooling rate 5°C/min are shown in Figure 4.5. The patterns of BDT ceramics were nearly identical to their own powders but with a little sharper peaks due to larger crystallite size. The XRD pattern of PZT ceramic, however, indicated that rhombohedral phase disappeared and only tetragonal phase (matched with ICSD file number 92059 of $Pb(Zr_{0.52}Ti_{0.48})O_3$ [102] was presented. This result could be attributed that the Zr/Ti ratio were changed between sintering process. From Figure 4.5, the starting with pure PZT phase, addition of 10 wt% BDT (0.9PZT–0.1BDT) into this compound caused a slight shift of all peaks to the right while the tetragonal structure was maintained. The possible reason could be attributed to the partial dissolution of BDT into PZT structure. Based on the ionic radius of Bi^{3+} ion (r_{Bi}^{3+} = 1.03 Å) and Dy^{3+} ion (r_{Dy}^{3+} = 0.912 Å), it would preferentially substitute Pb^{2+} (r_{Pb}^{2+} = 1.19 Å) site, while the Ti^{4+} ion (r_{Ti}^{4+} = 0.605 Å) may substitute for Ti^{4+} (r_{Ti}^{4+} = 0.605 Å) site [109]. This ion diffusion can result in a shift of the PZT diffraction peaks toward higher angles, which implies that the lattice constant of PZT phase may be decreased. However, the dissolution of BDT into PZT lattice may not be complete due to a present of main peak (117). It seemed that 0.9PZT–0.1BDT is a solubility limit of BDT in PZT.

The X-ray diffraction patterns from sintered PZT–BDT ceramics were formed throughout the whole composition range. The XRD patterns of the composites show a combination between PZT and BDT patterns. As the amount of BDT was increased to 30 wt% (0.7PZT–0.3BDT) as shown in Figure 4.5, peaks of PZT phase were maintained while peaks of BDT phase started to appear. An increase in BDT

concentration to 50 wt% (0.5PZT–0.5BDT), the patterns showed mixed phase between PZT and BDT. Increasing of 70 wt% BDT (0.3PZT–0.7BDT) caused peak shift in BDT. In addition, increasing BDT concentration up to 90 wt% (0.1PZT–0.9BDT) indicated a systematic shift of X-ray peaks. Nevertheless, this peak shifted could be identified as orthorhombic distortion of BDT phase. However, in this reportedwork, small amount of second phase (*) correlating with $Pb_2Bi_4Ti_5O_{18}$ compound (matched with ICSD file number 150403 [110] could be detected by XRD in the composition x = 0.3 up to 0.9.

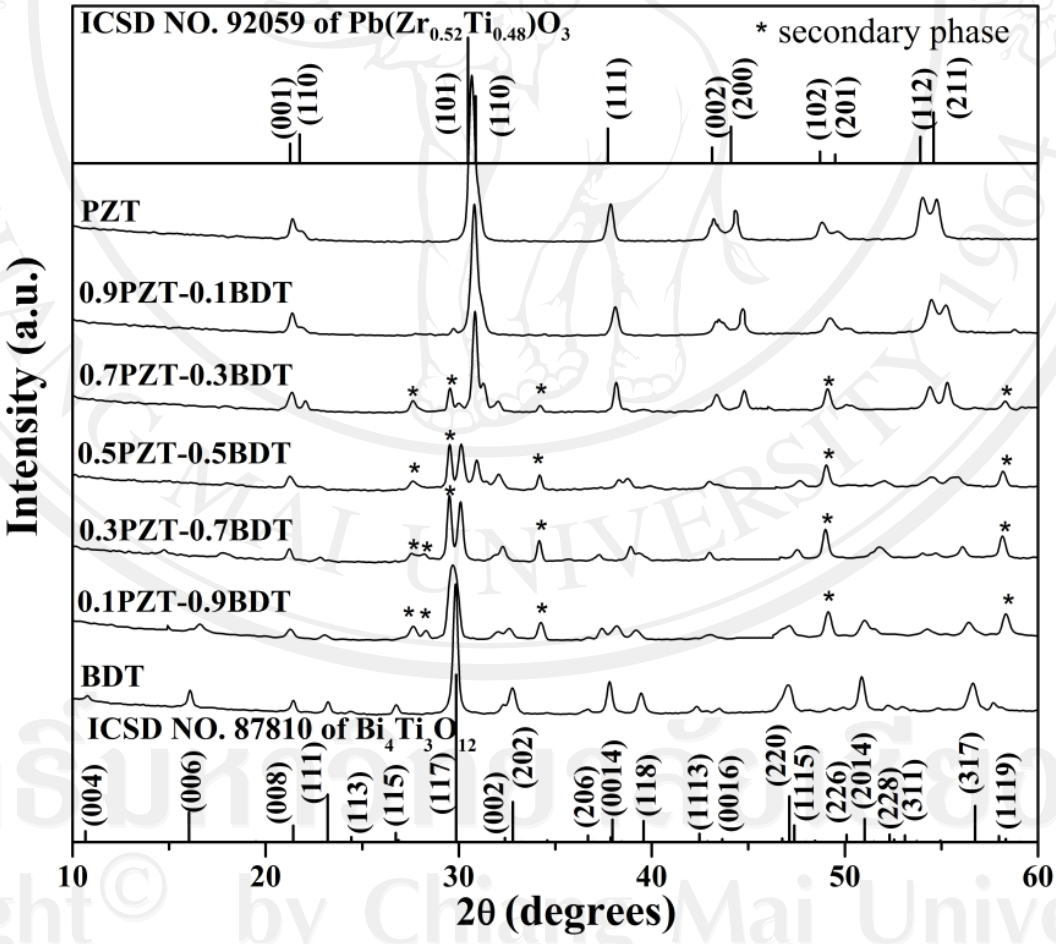

Figure 4.5 X-ray diffraction patterns of (1-*x*)PZT–*x*BDT ceramics.

4.2.3 Microstructural analysis of PZT–BDT ceramics

SEM micrographs of (1-*x*)PZT–*x*BDT ceramics are shown in Figure 4.6. The PZT ceramic had more equiaxed grains while BDT had plate-shaped grains, as shown in Figure 4.6(a) and (g), respectively. As the amount of BDT increased to 10 and 30 wt%, it was found that grain size decreased rapidly as shown in Figure 4.7. When BDT concentration was increased to 50 wt% (0.5PZT–0.5BDT), the ceramic consisted of both equiaxed and plate-like grains as shown in Figure 4.6(d). The values of plate thickness were measured along with plate length as present in Table 4.2. Both length and thickness of (1-*x*)PZT–*x*BDT ceramics (x = 0.5, 0.7 and 0.9) were found to increase with increasing BDT concentration.

It could be seen from SEM micrographs that addition of BDT into PZT, or vice versa, caused the porosity to increase. This could therefore be correlated to the density values obtained, as shown in Figure 4.8. The PZT-rich ceramics possessed high densities due to their more equiaxed grains, which could be packed to high density. On the other hand, the BDT-rich ceramics contained plate-shaped grains which could have different orientation of plate stacking, resulting in higher concentration of pores and thus lower densities. For pure BDT ceramic (as shown in Figure 4.6(g)), although the grains shape were plate-like, the density showed higher than BDT-rich ceramics. This could be a result of homogeneity and preferred orientation of grains, which could be more easily packed and caused the porosity to decrease and gave higher density.

Based on SEM micrographs, the PZT-rich ceramics show only equiaxed grains shape owing to the formation and development of complex structure is strongly dependent on the concentration of secondary phase and the sintering temperature. Because of the PZT matrix tended to restrain the growth of secondary phase, thus

making it was hard to observe the plate-like grains when the concentration of BDT was low [111], while the plate-like grains shape well was dominated at the BDT-rich ceramics. This result was corresponding to the result from X-ray diffraction analysis. Moreover, the results revealed that grain size of pure PZT and pure BDT ceramic larger than PZT–BDT ceramic. This result can be attributed that the presence of the second phases may affect the rate of grain growth depending upon their formation kinetics.

Figure 4.9 shows the fractured surface of (1-*x*)PZT–*x*BDT ceramics. The pure PZT and 0.9PZT–0.1BDT ceramics showed inter-granular mode, as shown in Figure 4.9(a) and (b). An increasing of BDT content (x = 0.3-1.0), the mixed between inter/trans-granular mode was presented. The main reason of this behavior might be inhomogeneity and different orientation of plate-like grains.

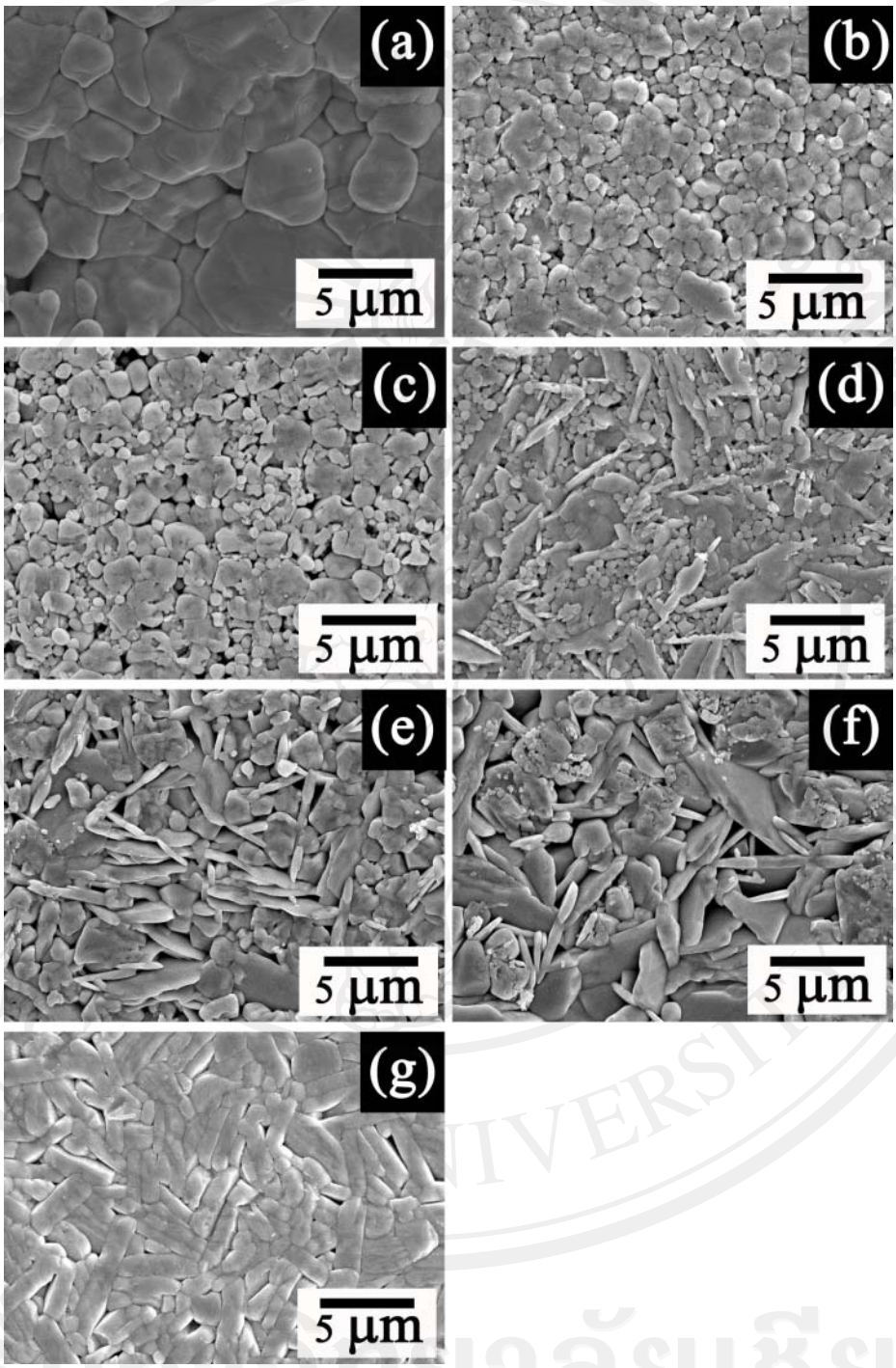

Figure 4.6 SEM micrographs of (1-*x*)PZT–*x*BDT ceramics sintered at 1000°C, where (a)-(g) represent *x* = 0, 0.1, 0.3, 0.5, 0.7, 0.9 and 1.0, respectively.

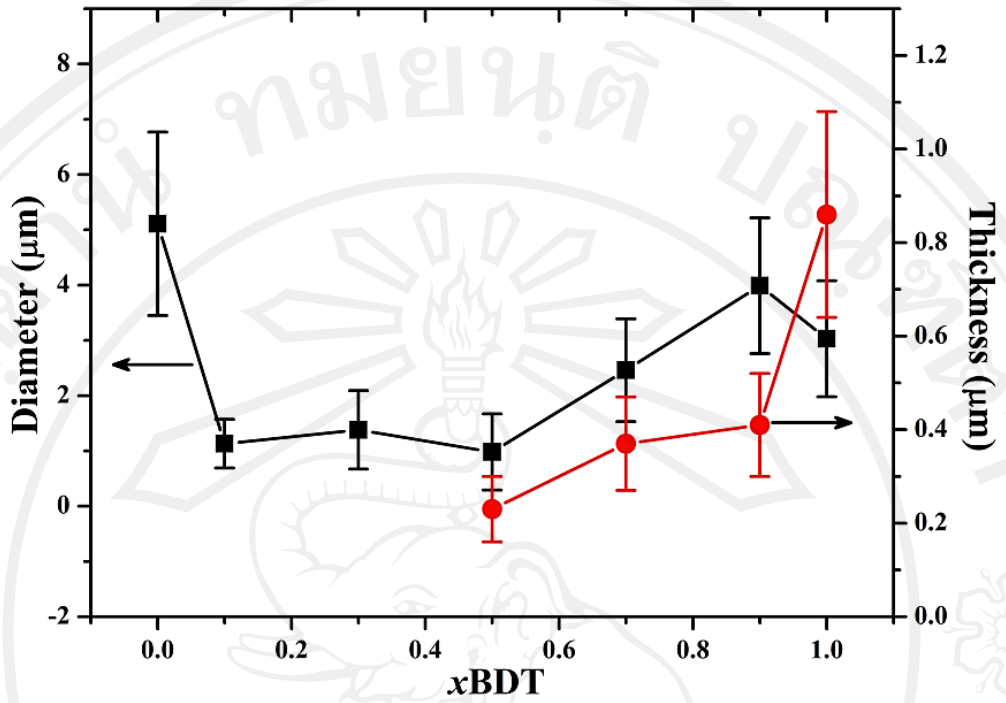

Figure 4.7 Relationship between grain size (diameter and thickness) and BDT content of (1-*x*)PZT–*x*BDT ceramics.

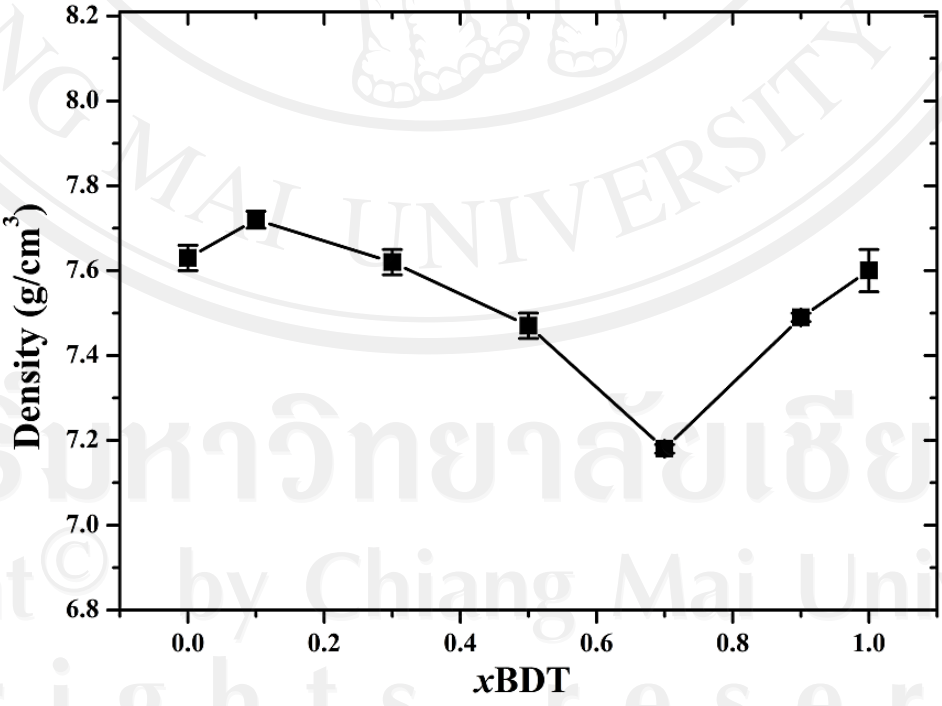

Figure 4.8 Plots of density as a function of BDT content.

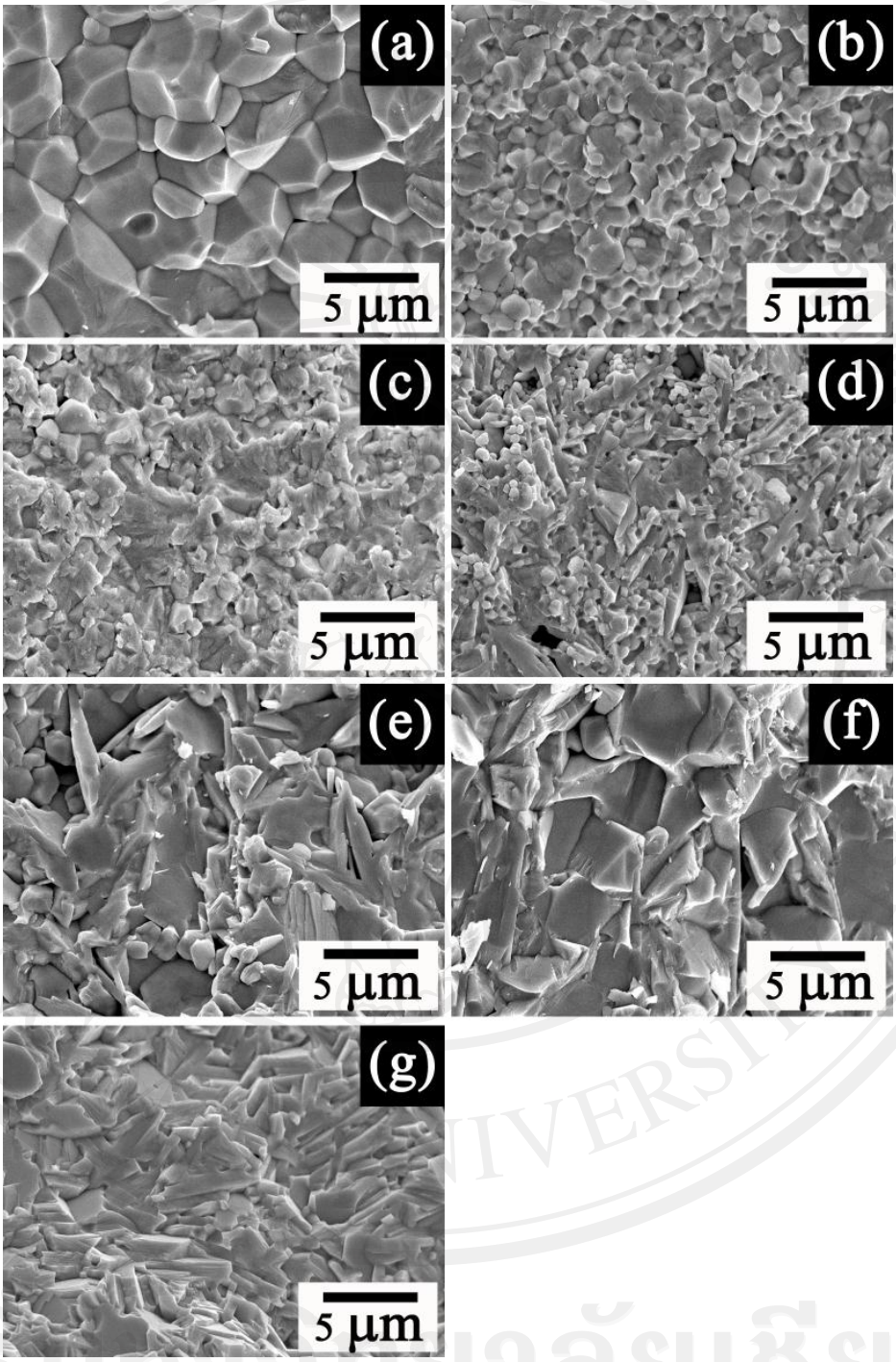

Figure 4.9 The fracture surface transferred of (1-*x*)PZT–*x*BDT ceramics sintered at 1000°C, where (a)-(g) represent *x* = 0, 0.1, 0.3, 0.5, 0.7, 0.9 and 1.0, respectively.

Table 4.2 Grain size of (1-*x*)PZT–*x*BDT ceramics sintered at 1000°C.

(1-*x*)PZT–*x*BDT	Grain size (μm)		
	Diameter (ϕ)	Thickness (t)	ϕ/t
PZT	5.11 ± 1.66	-	-
0.9PZT–0.1BDT	1.13 ± 0.44	-	-
0.7PZT–0.3BDT	1.38 ± 0.71	-	-
0.5PZT–0.5BDT	0.98 ± 0.69	0.23 ± 0.07	4.26
0.3PZT–0.7BDT	2.46 ± 0.93	0.37 ± 0.10	6.65
0.1PZT–0.9BDT	3.99 ± 1.23	0.41 ± 0.11	9.73
BDT	3.03 ± 1.05	0.86 ± 0.22	3.52

4.2.4 Electrical properties of PZT–BDT ceramics

Dielectric properties of (1-*x*)PZT–*x*BDT ceramics sintered at 1000°C were investigated. The room temperature dielectric properties were measured as a function of BDT content at frequency of 10 kHz as shown in Figure 4.10. The values related to the dielectric properties are also listed in Table 4.3. The maximum of dielectric constant was found in the pure PZT ceramic (ε_r = 929). A decrease of the dielectric constant values as a function of the BDT content can be seen in Figure 4.10. An increase in the BDT fraction caused the dielectric constant of the ceramic decreased gradually. This was probably resulted from the introducing of low dielectric material (BDT) in the ceramics. Therefore, the lower dielectric constant showed in the ceramics with higher concentrations of BDT. Moreover, the dielectric response of composite materials is another reason for explaining. Ausloos *et al.* [112] studied effective dielectric constant theories of composite solids. Their work reported that the results of clustering effect including the shape of the cluster and particle heterogeneity

effect. In this work, it is possible that BDT particles in the samples may hinder domain wall motion and lead to reduce dielectric constant.

Dielectric loss of (1-*x*)PZT–*x*BDT ceramics tends to increase with increasing BDT concentration from $x = 0$ to $x = 0.5$ and the highest dielectric loss of the ceramics was observed at $x = 0.5$ (0.5PZT–0.5BDT). This result was attributed to different of grain shapes between PZT and BDT, therefore, possibility to packing could be hard resulting to low density and poor homogeneity of microstructure. For higher concentration ($x = 0.7$-0.9), the dielectric loos decreased slightly due to the density of ceramics were increased. However, the dielectric loss increased in BDT ceramic. It is well known that the dissipation in ferroelectric materials occurs due to various causes such as space charge accumulation at grain boundaries and conductivity [113]. The presence of oxygen vacancies which act as space charge and contribute to the electrical polarization can be related to the dielectric loss [45, 114]. Therefore, BDT ceramic showing high dielectric loss could be attributed to high electrical conductivity of bismuth titanate based ceramics [115-117].

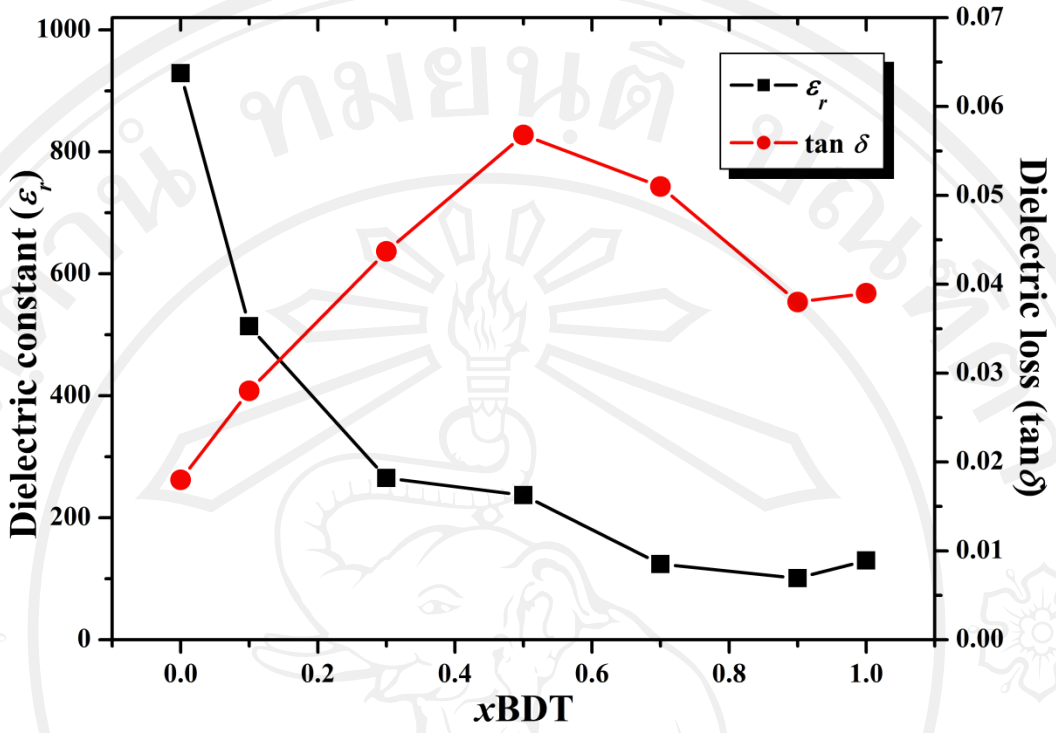

Figure 4.10 Plot of the dielectric properties as a function of BDT concentration.

Table 4.3 The dielectric properties of (1-*x*)PZT–*x*BDT ceramics measured at room temperature at a frequency of 10 kHz.

(1-*x*)PZT–*x*BDT	Dielectric constant (ε_r)	Dielectric loss (tanδ)
PZT	929	0.018
0.9PZT–0.1BDT	514	0.028
0.7PZT–0.3BDT	265	0.044
0.5PZT–0.5BDT	237	0.057
0.3PZT–0.7BDT	124	0.051
0.1PZT–0.9BDT	101	0.038
BDT	130	0.039

4.2.5 Ferroelectric properties of PZT–BDT ceramics

Polarization-electric field (*P*-*E*) hysteresis loops of (1-*x*)PZT–*x*BDT ceramics at a frequency of 50 Hz are presented in Figure 4.11 and 4.12. An empirical relationship between remanent polarization (P_r), maximum polarization (P_{max}) and polarization at a field above a coercive field was derived by Haertling *et al.* [118]. The hysteresis loop became slimmer with increasing BDT concentration. The ferroelectric parameters have been extracted from the experimental data, as summarized in Table 4.4. The ferroelectric characteristics can be assessed with the hysteresis loop squareness (R_{sq}) [119], which can be calculated from the following equation:

$$R_{sq} = \frac{P_r}{P_{\max}} + \frac{P_{1.1Ec}}{P_{\max}} \qquad (4.1)$$

where R_{sq} is the squareness of hysteresis loop, P_{max} is the polarization value at the maximum applied field obtained at some finite field strength below the dielectric breakdown and $P_{1.1Ec}$ is the polarization at an electric field equal to 1.1 times the coercive field (E_c). For an ideal hysteresis loop, R_{sq} is equal to 2.0 [118].

The polarization loop of pure PZT sample showed values of the coercive field (E_c) ~ 1.81 kV/mm and the remanent polarization (P_r) ~ 9.26 μC/cm^2. Addition of small amount of 10 wt% BDT (0.9PZT–0.1BDT) improved ferroelectric properties with 12.42 μC/cm^2 of the remanent polarization, 1.68 kV/mm of the coercive field and 0.84 of loop squareness. It is well known that the materials for memory applications are required to possess the following properties such as a large remanent polarization (P_r), a low coercive field (E_c) and high degree of loop squareness (R_{sq}) [1, 48, 50]. From the results, therefore, 0.9PZT–0.1BDT ceramic could be improved

ferroelectric properties. This seemed to be the effect of better homogeneity and uniformity of grain size [1], agreed with SEM investigation (as shown in Figure 4.6(b)), highest density, agreed with densification investigation (as shown in Table 4.1) and small content of secondary phase, according to XRD investigation (as shown in Figure 4.5) of this composition. However, increasing of BDT content gradually degraded ferroelectric properties of ceramics as shown in Figure 4.13. An addition of 50 wt% BDT into PZT showed very small degree of loop squareness with large coercive field (E_c) but small remanent polarization (P_r). The slim loop could be explained by the mixed phase of solid solutions between PZT and BDT which need much larger field to open up loops [31, 120]. Moreover, in this sample, both low density and high content of secondary phase together with the heterogeneous microstructure seemed to play a crucial role in the reduction ferroelectric behavior.

Figure 4.14 shows plot of normalized coercive field and loop squareness of the ceramics as a function of BDT content. Because of an applied filed dependence of ferroelectric properties of the ceramic [121, 122], this parameters has been normalized in a form of E_c/E_{max} values. The normalized coercive field and loop squareness showed similar trend where the values degraded with increasing of BDT content, as summarized in Table 4.4. It is possible that this lower ferroelectric property of these compositions was due to the heterogeneous microstructure. Moreover, the domain switching seemed to play a role in this degraded ferroelectric behavior. The domain switching was prevented by the second phase particles which were incorporated within the matrix grain, in agreement with earlier works [123, 124] led to hard switching of the domains.

Table 4.4 Ferroelectric properties of (1-*x*)PZT–*x*BDT ceramics.

(1-*x*)PZT–*x*BDT	P_r (μC/cm^2)	P_{max} (μC/cm^2)	R_{sq}	E_c/E_{max}
PZT	9.26	12.88	0.87	0.52
0.9PZT–0.1BDT	12.42	18.22	0.84	0.48
0.7PZT–0.3BDT	7.38	11.90	0.84	0.49
0.5PZT–0.5BDT	1.13	5.06	0.34	0.18
0.3PZT–0.7BDT	1.09	2.99	0.51	0.33
BDT	1.31	4.42	0.48	0.26

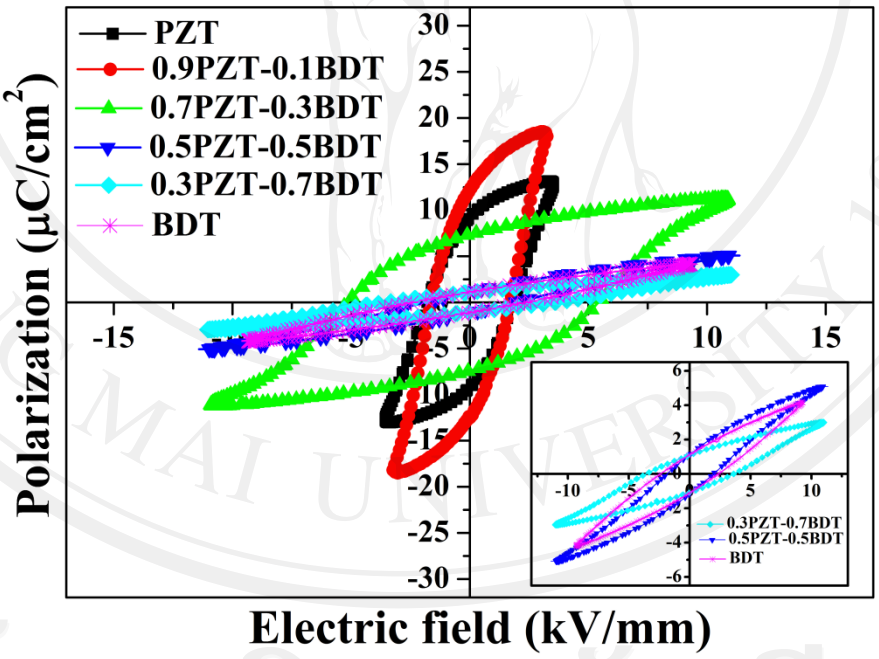

Figure 4.11 Comparison of polarization-electric field (*P*-*E*) hysteresis loops of (1-*x*)PZT–*x*BDT ceramics.

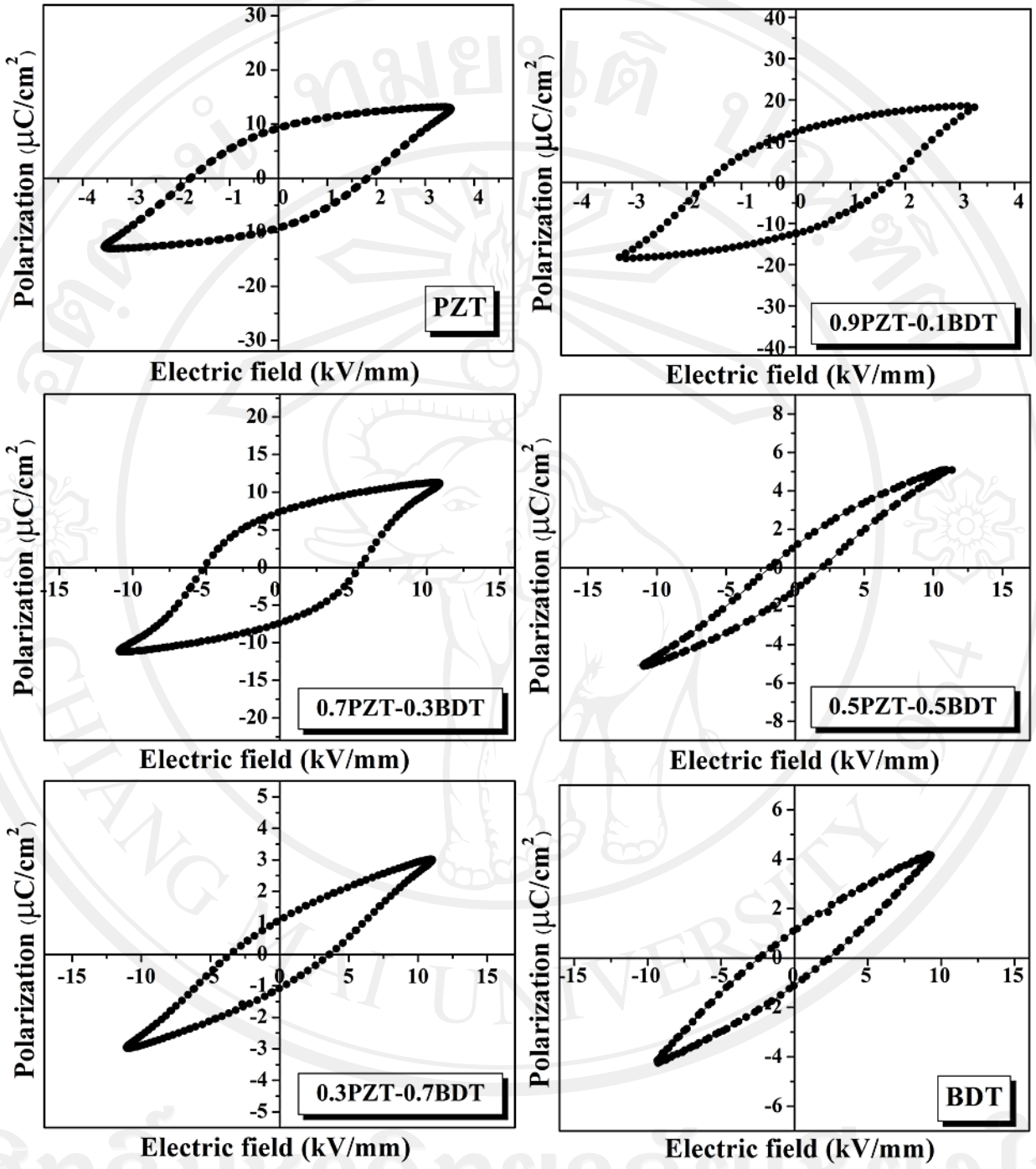

Figure 4.12 Polarization electric field (*P-E*) hysteresis loops of (1-*x*)PZT–*x*BDT ceramics.

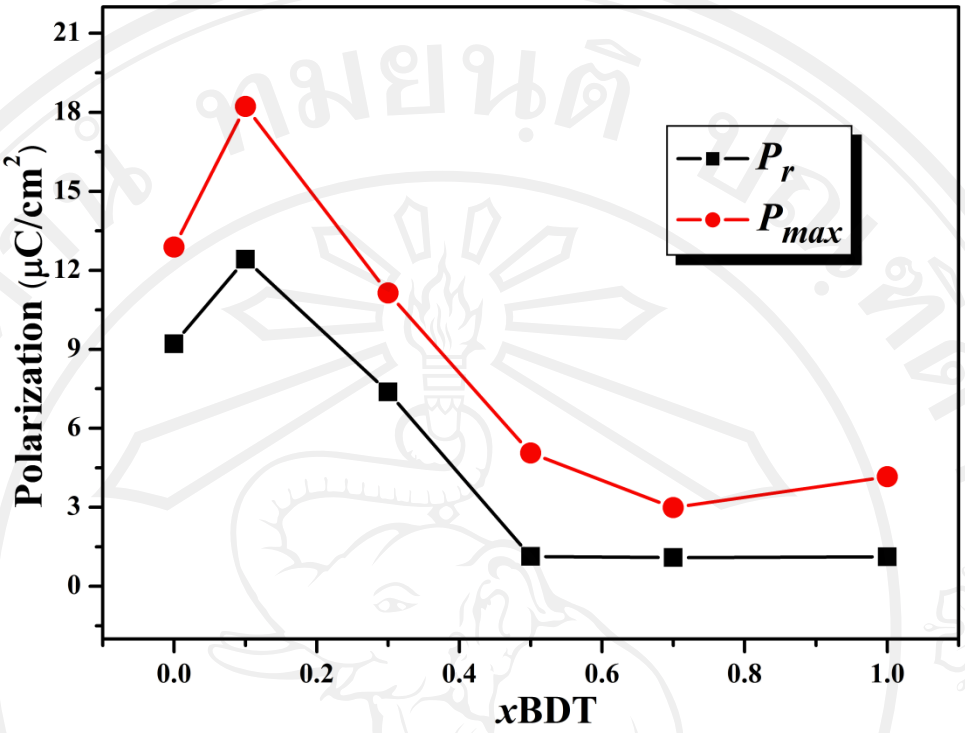

Figure 4.13 Plots of polarization as a function of BDT concentration.

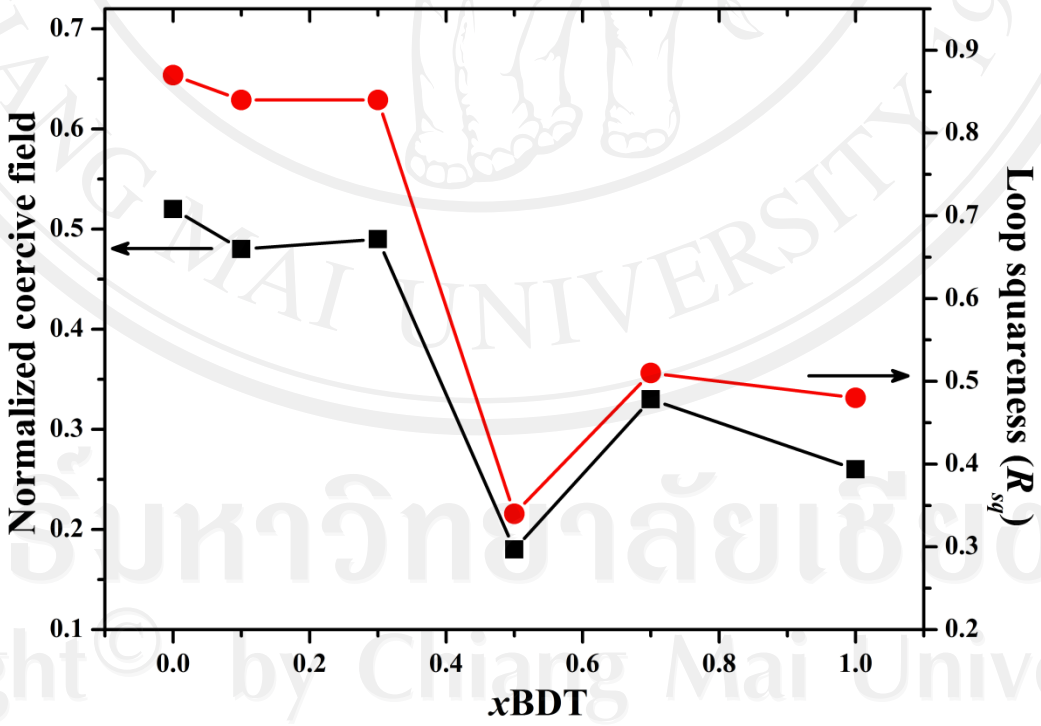

Figure 4.14 Relationship of ferroelectric parameters E_c/E_{max} and R_{sq} with BDT content.

4.2.6 Fatigue properties of PZT–BDT ceramics

Hysteresis loops of (1-*x*)PZT–*x*BDT ceramics before and after 10^6 polarization switching cycles were compared in Figure 4.15. The samples were electrical fatigued under an applied field of higher than 1.4 times of a switching electric field (E_{sw}) and a fixed frequency at 50 Hz. The results showed that dramatic drop of polarization value was observed for pure PZT ceramic. Addition small amount of BDT into PZT (0.9PZT–0.1BDT) could be improved degradation of remanent polarization. Much smaller changes of hysteresis loops was observed in the sample with 30 wt% BDT additions (0.7PZT–0.3BDT). Increasing BDT content to more than 30 wt% resulted in almost no degradation of ferroelectric properties. This was probably resulted from the introducing of bismuth layered material (BDT) which possesses high fatigue endurance and it will be explained in next section.

Figure 4.16(a) and (b) shows variation tendency of positive and negative remanent polarization of the PZT–BDT ceramics plotted as a function of number of switching cycles at a measurement of 50 Hz. For pure PZT ceramic, remanent polarization decreased from 9.26 to 4.27 μC/cm^2 (see Table 4.5) after 10^6 polarization switching cycles. The remanent polarization before electrical fatigue was increased to 12.42 μC/cm^2 in 0.9PZT–0.1BDT sample, indicating a maximum value of the ceramic system. After 10^6 polarization switching cycles, remanent polarization was decreased to 7.19 μC/cm^2. The result revealed that the fatigue behavior was improved. Addition of 30 wt% BDT (0.7PZT–0.3BDT) caused a slight decrease in remanent polarization with low degradation of ferroelectric properties observed after electrical fatigue. As BDT content in PZT–BDT ceramics increased to 50 wt% (0.5PZT–0.5BDT),

remanent polarization dropped significantly to ~1 μC/cm^2 with almost no degradation of remanent polarization observed after electrical fatigue.

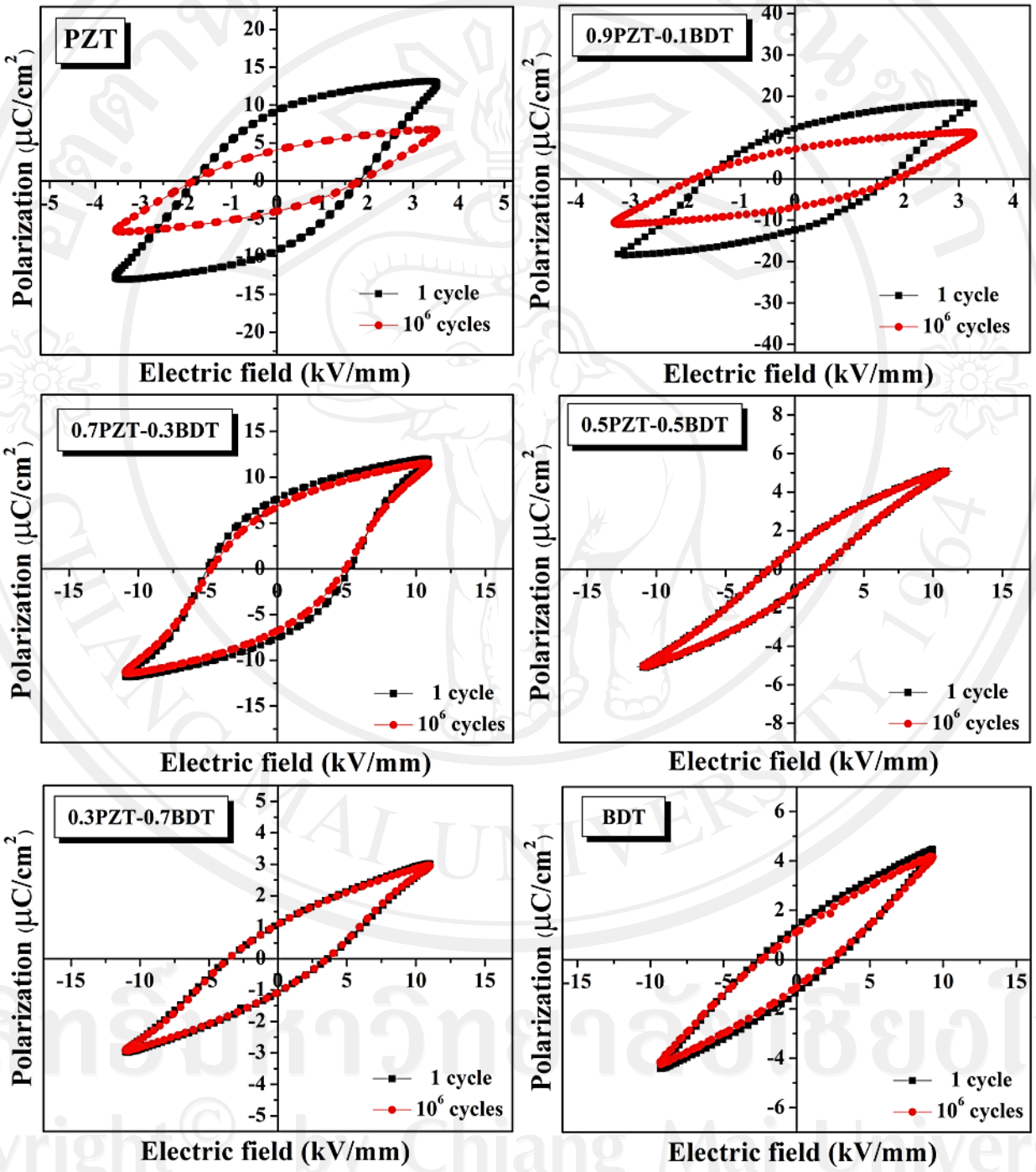

Figure 4.15 Polarization-electric (*P-E*) loops of (1-*x*)PZT–*x*BDT ceramics before (■) and after (●) electrical fatigue 10^6 switching cycles.

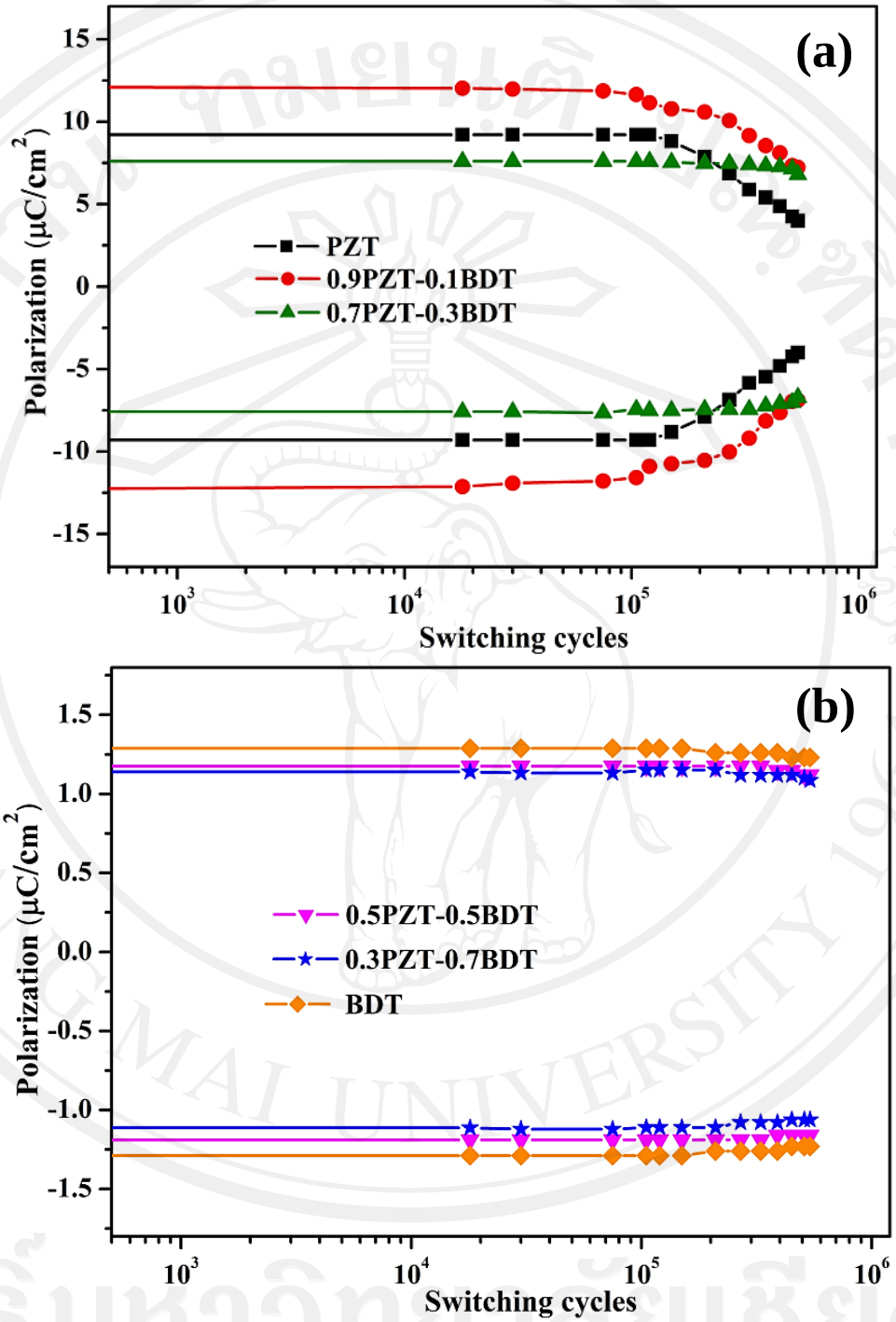

Figure 4.16 The variation of positive and negative remanent polarization of (1-*x*)PZT–*x*BDT ceramics as a function of the number of switching cycles at a frequency of 50 Hz (a) x = 0, 0.1 and 0.3 (high remanent polarization) and (b) x = 0.5, 0.7 and 1.0 (low remanent polarization).

From Figure 4.17, the normalized of remanent polarization was plotted as a function of switching cycles. The remanent polarization was decreased to 56% and 42% of the original value after 10^6 switching cycles for pure PZT and 0.9PZT–0.1BDT ceramics, respectively. A further increase in BDT ≥ 30 wt%, resulted in almost no change in ferroelectric values after electrical fatigue. Based on X-ray diffraction analysis, the orthorhombic phase of bi-layered material appeared in the 0.7PZT–0.3BDT ceramic. Hence, improved fatigue endurance due to an addition of bi-layered structure compound was clearly observed.

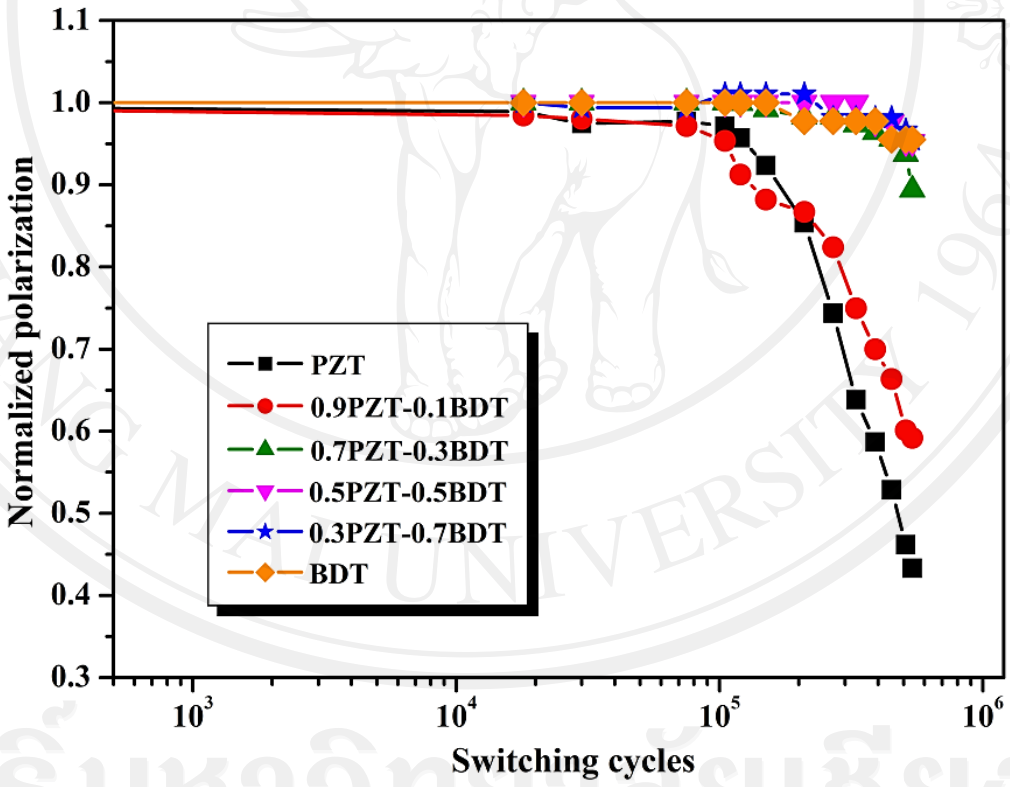

Figure 4.17 The normalized of remanent polarization of the (1-*x*)PZT–*x*BDT ceramics as a function of the number of switching cycles at a frequency of 50 Hz.

The results revealed that pure PZT ceramic had severe polarization fatigue. It has been widely accepted that polarization fatigue of the PZT mainly originates from accumulation of oxygen vacancies and domain wall pinning [88, 125-127]. During reorientation of ferroelectric domains in the fatigue process, oxygen vacancies was driven towards ferroelectric domain walls or grain boundaries and captured by space charge over there. The heavy pile-up of captured oxygen vacancies at those sites would lead to an increasing domain wall pinning rate and thus preventing further domain switching [126, 128]. In contrast to PZT, BDT ceramic exhibited no fatigue at least up 10^6 switching cycles. For BDT ceramic and other bi-layered perovskite ferroelectric, there are several reasons responsible for the fatigue-free behavior: (i) the unpinning domain rate of domain walls is larger than the pinning rate, resulting in the fact that the domain are easily switched [129], (ii) the $(Bi_2O_2)^{2+}$ layers in bi-layered perovskite structure can provide a net pool to compensate for the charge accumulation [130] and (iii) better chemical stability of the perovskite layers against oxygen vacancies after substitution of some Bi atoms by Dy atoms improves fatigue behavior [9, 55, 131]. The improved fatigue properties in PZT–BDT ceramics compared to the pure PZT structure could be attributed to the oxygen vacancies in the PZT layer absorbed by $(Bi_2O_2)^{2+}$ layers in the bi-layered perovskite structure of BDT layer. Besides, the relative small remanent polarization of the PZT–BDT structure will result in a smaller electrostatic role to the trap depth for charges at domain boundary. This result possibly weakens the pinning of domain walls and thus leads to higher unpinning rate [132]. However, 0.9PZT–0.1BDT ceramic belongs to PZT solid solution phase improved fatigue endurance. This result can be attributed that the addition of small amount of BDT to PZT also greatly reduces fatigue, according with

phase analysis in this system which Bi atoms of BDT could be diffuse into the PZT layer, in agreement with other work [133].

Table 4.5 Ferroelectric properties of (1-*x*)PZT–*x*BDT ceramics measured before and after electrical fatigue tests.

(1-*x*)PZT–*x*BDT	P_r (μC/cm^2)			P_{max} (μC/cm^2)		
	1 cycle	10^6 cycles	% of decrease	1 cycle	10^6 cycles	% of decrease
PZT	9.26	4.07	56	12.88	6.52	49
0.9PZT–0.1BDT	12.42	7.19	42	18.22	10.98	40
0.7PZT–0.3BDT	7.38	6.78	8	11.90	11.37	4
0.5PZT–0.5BDT	1.18	1.13	4	5.10	5.06	1
0.3PZT–0.7BDT	1.14	1.09	5	2.99	2.98	1
BDT	1.29	1.23	5	4.42	4.19	5

4.3 Conclusions of PZT–BDT system

New complex-structured $(1-x)Pb(Zr_{0.52}Ti_{0.48})O_3–x(Bi_{3.25}Dy_{0.75})Ti_3O_{12}$ ceramics were successfully prepared. PZT ceramic was identified by X-ray diffraction method as a single-phase material with perovskite structure having tetragonal phase. Addition of 10 wt% BDT in PZT ceramics resulted in a distorted tetragonal crystal structure. While, an addition of 10 wt% PZT in BDT ceramics caused the structure to be mainly distorted orthorhombic BDT-like structure. Optimum sintering temperature for this system was found to be 1000°C in air for 4 h with a heating/cooling rate 5°C/min. The highest density was achieved at 0.9PZT–0.1BDT ceramic. Further increasing the content of BDT gradually decreased densities of the ceramics. Microstructure of PZT–BDT ceramics showed that pure PZT ceramic had more equiaxed grains while BDT ceramic were plate-shaped grains. The microstructure evolution in this ceramic system was in agreement with X-ray diffraction analysis. The PZT–BDT ceramics were demonstrated to possess improved fatigue characteristics over pure PZT ceramics. The samples with BDT content > 30 wt% showed almost no degradation of ferroelectric properties. Although, dielectric constant of PZT ceramic was reduced by an addition of BDT, the PZT–BDT ceramics showed larger remanent polarization than pure PZT ceramic. These results revealed that this new ceramic system has synergically combined the individual advantages of PZT and BDT ceramic together, i.e. good dielectric properties of PZT ceramic and good fatigue endurance of BDT ceramics.